Nanoscale

PAPER

View Article Online
View Journal | View Issue

Cite this: *Nanoscale*, 2025, **17**, 25187

Selective enhancement of graphene ammonia sensing by electrochemical palladium nanoparticle decoration: *ab initio* insights into the sensing response

Sonia Freddi, *[a,b] Pilar Carro, [c] Alberto Hernández Creus,[c] Luigi Sangaletti [b] and Miriam C. Rodriguez Gonzalez*[c]

A simple and cost-efficient approach has been proposed for the decoration of graphene with the aim of enhancing its gas sensing performance. Pd NP-decorated graphene has been prepared through electrodeposition, with the number and the size of the particles being tuned by controlling the time and potential applied, respectively. After characterization, the four prepared layers and a pristine one have been tested towards several gases, including ammonia and nitrogen dioxide. The study demonstrates that graphene chemiresistors exhibit excellent sensitivity, stability up to 5 months, and competitive detection limits for ammonia. Selectivity towards ammonia over nitrogen dioxide, acetone, 2-propanol, ethanol, and water vapor was confirmed, with decorated graphene sensors showing enhanced ammonia response compared to pristine sensors. A systematic analysis revealed that smaller Pd NPs and higher coverage significantly improve ammonia sensing, offering potential for advanced Pd NP-decorated sensor development. Finally, density functional theory (DFT) calculations provided the theoretical framework to rationalize the sensing mechanism and explain the selective enhancement of the sensing performance towards ammonia exposure for the Pd NP-decorated layers compared to the pristine one.

Received 14th June 2025,
Accepted 1st October 2025

DOI: 10.1039/d5nr02547h

rsc.li/nanoscale

Introduction

Monitoring ammonia is imperative for a multitude of applications due to its substantial impact across diverse sectors, including agriculture, industry, medicine, and the environment. In the agricultural sector, ammonia monitoring is crucial for the assessment and optimization of fertilizer usage,[1] with the aim of preventing over-application, which can lead to soil and water contamination.[2] In industrial settings, particularly in manufacturing and chemical processing, continuous monitoring of ammonia levels is essential for ensuring worker safety, as high concentrations can pose serious health hazards.[3,4] Additionally, in the context of air quality monitoring, tracking ammonia is paramount to comprehending its role in atmospheric pollution, as ammonia is one of the precursors of fine particulate matter,[5] and a contributor to acid rain.[6] In the food industry, ammonia can be tracked to assess the quality and freshness of meat.[7] Finally, ammonia also plays a pivotal role in breath analysis, serving as a biomarker for liver and kidney pathologies,[8] as well as for chronic obstructive pulmonary diseases.[9] These applications share the common fact that concentrations of ammonia to be detected are very low, typically in the ppb to low ppm range. Consequently, there is a growing demand for the development of competitive gas sensors capable of detecting these low ammonia concentrations.

In recent decades, significant research interest has been directed towards graphene for a variety of applications, including gas sensors. Indeed, exploitation of graphene has begun for its use as a sensing material, owing to its outstanding electrical properties, which include high in-plane conductivity,[10] low electrical intrinsic noise,[11] excellent chemical stability at room temperature,[12] and strong sensitivity to gas molecule adsorption on its surface.[10] Despite its exceptional characteristics, pristine graphene does not exhibit significant performance as a gas sensor; rather, functionalization or decoration is required to enhance its sensing capabilities.[13–17]

Recent advancements have also demonstrated that other graphene derivatives and graphene-based composites can

[a]*Institute of Photonics and Nanotechnologies - Consiglio Nazionale delle Ricerche (IFN CNR), Laboratory for Nanostructure Epitaxy and Spintronics on Silicon (LNESS), Via Anzani 42, 22100 Como, Italy. E-mail: sonia.freddi@cnr.it*
[b]*Surface Science and Spectroscopy Lab at I-Lamp, Department of Mathematics and Physics, Università Cattolica del Sacro Cuore, via della Garzetta 48, 25133 Brescia, Italy*
[c]*Área de Química Física, Departamento de Química, Instituto de Materiales y Nanotecnología (IMN), Universidad de La Laguna (ULL), 38200 La Laguna, Spain. E-mail: mrodrgon@ull.edu.es*

achieve excellent sensing performance. For example, reduced graphene oxide functionalized with metal oxides or polymers or transition metal dichalcogenides has been reported to deliver high sensitivity, fast response/recovery times and promising detection limits, taking advantage of the combined effects of graphene conductivity and catalytic or adsorption properties of the functionalized material.[18–22]

Noble metal nanoparticles (NPs) have been utilized to enhance the sensing capabilities of nanostructured carbon due to their substantial surface area, efficient electron transfer properties, and high catalytic activity.[23,24] Specifically, the objective of functionalizing carbon-based materials with metal NPs is to enhance the surface reactions and promote electron transfer between the gas molecule and the carbon-based surface.

In the case of carbon nanotubes (CNTs), it has been reported that small gas molecules can form strong bonds with metal NPs due to their electronic structure and available empty orbitals.[25] Hence, coupling CNTs with metal NPs can enhance the electrical properties and sensitivity of CNTs by increasing the number of adsorption sites available for target gas interactions.[26] Among all the noble metal NPs that have been utilized for the purpose of decorating CNTs, *i.e.* Au, Pt, Pd, Rh, and Ag, Pd NPs have been identified as particularly promising for hydrogen and ammonia detection.[23,24,27]

It is hypothesized that Pd NPs will act in a manner analogous to that of CNTs utilized for the purpose of decorating graphene. In particular, it has been demonstrated that Pd NPs can significantly enhance the detection of hydrogen, when decorating graphene or reduced graphene oxide.[28,29] However, evidence regarding ammonia enhancement remains elusive. In this study, we propose a Pd NP decoration of graphene employing electrochemistry to develop highly sensitive ammonia sensors. The Pd NPs are deposited using electrochemical methods due to the versatility and control that these methods offer. The control of the density of particles, their sizes and shapes can be achieved by tuning potential and time conditions during the electrolysis.[30,31] In particular, we studied the efficiency of Pd NPs deposited on graphene as a sensing material and we analyzed the effect of time and applied potential in the electrodeposition of the Pd NPs on the response toward ammonia detection. After thorough characterization utilizing XPS, AFM, and Raman spectroscopy, four NP-decorated samples and a pristine sample were arranged on a meticulously designed platform capable of concurrently monitoring the responses from all sensors. This platform enabled a straightforward comparison of the performances of all sensors under identical operating conditions.

Exposure to ammonia was conducted, resulting in the establishment of calibration curves for the five sensors. The prepared sensors have been shown to possess a very good degree of sensitivity towards ammonia in comparison with the results reported in the relevant literature. A notable limit of detection has been identified for the NP-decorated samples, in comparison with the pristine layer and the existing literature. Furthermore, the response and recovery times are consistent with those reported in the literature for graphene chemiresistors.

A systematic study of the effect of Pd particle size and coverage on ammonia sensing reveals that smaller NPs enhance ammonia sensing more effectively, while higher coverage leads to better performance when comparing samples with the same NP size. Furthermore, the stability of ammonia responses has been demonstrated, with responses remaining consistent for up to five months following sample preparation. To validate the selectivity of the sensors, exposures to interfering gases (*e.g.* nitrogen dioxide, ethanol, acetone, and 2-propanol) were performed. The response to volatile organic compounds (VOCs) was found to be negligible, while a low response was detected for nitrogen dioxide. This investigation further elucidates that the functionalization with palladium nanoparticles selectively enhances the response to ammonia.

Finally, DFT calculations have been performed to disclose the rationale behind the selective enhancement of ammonia detection after Pd NP decoration compared to nitrogen dioxide. The results suggest that the enhancement is related to the larger change induced in the palladium work function upon adsorption of ammonia.

Experimental

Materials

$PdCl_2$ (Sigma-Aldrich, 99.9%), $HClO_4$ (Merck, 70–72%), $NaClO_4$ (Sigma-Aldrich, 98%) and NaOH (Sigma-Aldrich; 99.99%) were used as received. Ultra-pure water (18.2 MΩ cm; Milli-Q, Millipore) was employed to prepare all the solutions. Before each measurement, argon (N50, Air Liquide) was bubbled through the solution to displace dissolved oxygen. A graphene monolayer on a silicon nitride/silicon substrate was purchased from Graphenea and used as received.

Sample preparation

Palladium nanoparticles (Pd NPs) were synthesized electrochemically as described previously.[31] Briefly, a three electrode cell was used. For this purpose, a graphene substrate as the working electrode, an Ag/AgCl electrode as the reference electrode and a platinum wire as the counter electrode were employed. Palladium electrodeposition was performed through a potential pulse from 0.80 V to −0.15 V or −0.60 V for the selected time (5 s or 20 s) on a graphene electrode immersed in 0.1 mM $PdCl_2$ + 0.1 M $NaClO_4$ + 1 mM $HClO_4$ solution. Four different samples were prepared: −0.15 V for 5 s (PdNPs_A), −0.15 V for 20 s (PdNPs_B), −0.60 V for 5 s (PdNPs_C) and −0.60 V for 20 s (PdNPs_D).

Sample characterization

To assess the chemical composition of the prepared samples, Raman spectroscopy and X-ray photoemission spectroscopy (XPS) measurements were carried out. Additionally, Raman spectroscopy provided information on the integrity of the graphene layer after the electrochemical process. Atomic force

microscopy (AFM) was carried out to gain information on the morphologies of the samples.

Raman spectra and maps were acquired on a CGS device with a Micro Raman Renishaw-InVia system, equipped with a 633 nm He–Ne laser source, using backscattering geometry. The laser light was focused onto the sample using a 100× objective (LEICA confocal microscope, N.A. 1.4) with 5 mW laser power and 1800 lines per mm grating. For the recording of a single spectrum, the acquisition time was set at 5s and the signal was accumulated 15 times. For Raman mapping, the acquisition time was set at 10s, while the signal accumulation number was set at 5.

A fully calibrated VG-Scienta R3000 spectrometer[32] was used to carry out the XPS investigation, using a non-monochromatic Al Kα line ($h\nu$ = 1486.6 eV) from a twin anode PsP X-ray source. The overall energy resolution was 0.85 eV. The spectra were acquired in transmission mode, at a power of about 30 W, with a pass energy setting of 100 eV for survey spectra, and 50 eV for core-level spectra.

The energy step was set at 0.5 eV and 0.1 eV for survey and core-level spectra, respectively. The chamber pressure during all measurements was within a range of 6.0×10^{-10} mbar to 7.5×10^{-10} mbar.

To interpolate the XPS data, homemade software, BriXias, written in IGOR PRO was used;[32,33] in detail, for the core-level fitting, Voigt functions were used. A couple of different areas were investigated for each sample, in order to assess the homogeneity of the prepared layers. Additionally, for each spot, the lateral resolution of the system is about 1 mm^2, which assures the reliability of the chemical investigation. AFM images were acquired with a Park NX 10 system in tapping mode at an air–solid interface and at room temperature. A PPP-NCHR tip (NanoSensors) working with a resonance frequency of about 300 kHz was used. All image processing was performed using Gwyddion software.[34]

Gas exposure

Silver paint electrical contacts were printed as thin stripes on opposite sides of a pristine sample and on the decorated layers. All samples were then mounted on an appropriately designed platform, capable of accommodating up to 8 sensors operating simultaneously, allowing for direct comparison of the behaviour of the sensors under the same environmental conditions.

Gas exposure was conducted at room temperature within a sealed chamber by introducing a mixture of synthetic air with a predetermined concentration of the gas molecule under investigation. To supply the chamber, two channels were used, connected to programmable mass-flow controllers that work in a 20–500 sccm range. The gas analyte cylinders (ammonia, nitrogen dioxide, *etc.*) and synthetic air used for all measurements were certified by S.I.A.D. Spa. The cylinder connected to the first mass-flow controller was loaded with the gas analyte under investigation, mainly ammonia (48 ppm in synthetic air), while the cylinder loaded with synthetic air alone was connected to the second mass-flow controller. Synthetic air was used to both purge the chamber after gas exposure and dilute the overall concentration of the gas analyte in the chamber; in the latter case, the air and analyte from both cylinders were premixed before entering the chamber. Temperature and R.H. values were monitored using two commercial sensors (humidity sensor HIH-4000 series Honeywell Sensing and Thermistor NTC PCB 5K Murata, respectively), mounted on the same board that accommodates the developed gas sensors. During all gas exposure tests, the overall R.H. was about 50 ± 10%. A scheme of the setup used for gas exposure tests is reported in the SI (Fig. S1a).

The graphene-based sensors presented in the manuscript work in a chemiresistor configuration, where the detection of the gas analytes is based on measuring the resistance changes of the sensing layers caused by their interaction with the gas molecules. The electronic circuit of each sensor is reported in Fig. S1b. A load resistor (R_L) is connected in series with the sensor, and when a constant voltage (V = 5 V) is applied, the output voltage (V_{OUT}) is monitored across the sample, providing the resistance value R of the sensor. The sensor response is here defined as $\Delta R/R_0 = (R - R_0)/R_0$, where R_0 represents the baseline sensor resistance before gas exposure and $\Delta R = R - R_0$ denotes the change in resistance value due to gas interaction. By carrying out several exposure tests, calibration curves for each sensor could be drawn by plotting the sensor response $\Delta R/R_0$ against the gas concentration.

Calculations based on density functional theory (DFT)

The calculations were performed using the projector augmented wave (PAW) method,[35] as implemented in the Vienna *ab initio* simulation package (VASP).[36–38] The valence electrons were described within a plane-wave basis set and an energy cutoff of 420 eV, while the remaining electrons were kept frozen as core states. Electron exchange–correlation was represented using the revised functional of Perdew, Burke and Ernzerhof with the Pade approximation (RP) of the Generalized Gradient Approximation (GGA).[39] The weak van der Waals forces were treated by the semi-empirical Grimme method (DFT-D) where the dispersion correction term was added to the conventional Kohn–Sham DFT energy[40] with the DFT-D3 parametrization.[41]

The energy convergence criterion was 10^{-5} eV for SCF energy. The atomic positions were relaxed until the force on the unconstrained atoms was <0.03 eV $Å^{-1}$. The calculated Pd lattice constant was 3.9059 Å, which compares reasonably well with the experimental value of bulk Pd (3.8907 Å).[42]

The Pd(111) surface was represented by five atomic layers, with a vacuum of ~20 Å separating any two successive slabs. Optimal Monkhorst–Pack[43] k-point grids of 9′9′1 and 5′9′1 were used for numerical integration in the reciprocal space of $(\sqrt{3}'\sqrt{3})$ $R30°$ and $(2\sqrt{3}'\sqrt{3})$ $R30°$ surface structures. Surface relaxation was allowed in the two uppermost Pd layers of the slab, and the atomic coordinates of the adsorbed species were allowed to relax without further constraints. Adsorbates were placed just on one side of the slab, and all calculations included a dipole correction. In the case of gas-phase species,

an orthogonal cell of appropriate size was employed. Spin polarization was considered for all gas-phase species.

The binding energies of the adsorbates were defined as follows,

$$E_b = E_{surface+ads} - E_{surface} - E_{ads} \quad (1)$$

where $E_{surface+ads}$, $E_{surface}$ and E_{ads} denote the total energy of the adsorbate–substrate system, the energy of the clean surface and the energy of the molecules in the gas phase, respectively. A negative number indicates that adsorption is exothermic with respect to the separate clean surface and the adsorbate in the gas phase.

The change in the work function, $\Delta\Phi$, caused by adsorption on the metal surface was defined as follows,

$$\Delta\Phi = \Phi_{surface+ads} - \Phi_{surface} \quad (2)$$

where Φ was evaluated as $\Phi = V_{vac} - \varepsilon_{Fermi}$, with V_{vac} being the averaged electrostatic potential in the vacuum gap of the supercell and ε_{Fermi} the slab Fermi level.

Results and discussion

As illustrated in Fig. 1a, the Raman spectra were collected from a pristine graphene layer (red trace) and from the decorated samples (yellow, blue, purple and green traces). In all the samples, the G and the 2D bands of graphene are clearly detected at 1587 cm^{-1} and 2636 cm^{-1}, respectively. The G-band is attributed to the in-plane stretching of sp^2 carbon atoms within the graphene lattice, while the 2D band is a second order Raman scattering process and is associated with the breathing mode of carbon atoms within the plane of graphene.[44] A visual analysis of the graphene spectrum reveals the presence of the D-band, indicative of defects, at approximately 1340 cm^{-1}. The relative intensity of the D and G bands is comparable in both pristine and decorated samples (approximately 0.57 ± 0.03 for pristine, and between 0.60 ± 0.02 for PdNPs_B and 0.54 ± 0.03 for PdNPs_C). This finding indicates that the potential damage to the graphene layer by the electrodeposition step is not significant.

The origin of the peaks at 1450 cm^{-1} and 1530 cm^{-1} is not completely clear. In the literature, they are assigned to graphene nanoribbons;[45] nevertheless, in those samples, those peaks are likely related to the corrugation of the graphene layer due to the wet transfer process.

To determine the type of doping of a graphene layer, the 2D Raman band position is usually tracked.[46] Thus, Raman maps of this band have been collected from several areas of the functionalized samples and the results, reported in Fig. S2, show that no significant shift towards higher or lower wavenumber is observed for the decorated samples compared to the Gr_pristine position, indicating that the functionalization does not alter the doping nature of graphene, although Pd NPs are expected to further enhance the p-type doping of graphene owing to their higher work function. This absence of a clear Raman signature may arise from the relatively low Pd coverage or the nanoscale distribution of NPs.

In Fig. 1b, a representative XPS spectrum acquired on the Pd NP-decorated layer is shown. The silicon nitride substrate contributes to the Si and N peaks,[47] while the graphene contribution is evident from the presence of the O 1s and C 1s peaks.[13,48] As clearly reported in Fig. 1c, the palladium core-level spectra collected on all the decorated samples present the same shape and composition. The XPS analysis reveals the presence of a metallic signal (BE = 339.9 eV and BE = 334.6 eV) and oxidized palladium,[49] which aligns with the well-known tendency of palladium to oxidize in air and the XPS sensitivity to the first nanometers of the investigated surface.

In detail, as reported in the right panel of Fig. 1c, it is possible to indicate each contribution of the Pd 3d core-level spectrum, starting from the binding energies for Pd $3d_{5/2}$ and Pd $3d_{3/2}$, which could be deconvoluted into three doublets.

The doublet peaks with the higher intensity are observed at binding energies of 334.6 eV (Pd $3d_{5/2}$) and 339.9 eV (Pd $3d_{3/2}$), and they are attributed to metallic palladium,[50,51] as mentioned earlier in the text. A second doublet, with binding energies of 335.4 eV (Pd $3d_{5/2}$) and 341.2 eV (Pd $3d_{3/2}$), is related to the presence of PdO, in particular to the Pd^{2+} state. The third doublet, with peaks at 337.0 eV (Pd $3d_{5/2}$) and 342.8 eV (Pd $3d_{3/2}$), is linked to the presence of PdO_2, thus to the Pd^{4+} state.[51,52]

All the areas of the doublets are in a 3 : 2 ratio, consistent with the spin–orbit coupling.

XPS analysis was performed to quantify the surface particle density, and several core-level spectra of C 1s and Pd 3d were collected on the decorated samples. The results of the quantification are reported in Table 1.

AFM images representative of the decorated layers are shown in Fig. 1d, while the size distribution of the NPs obtained from several AFM images is reported in Table 1 and Fig. S3.

Combining the results of XPS Pd/C ratio and AFM investigations, it is possible to conclude that, as expected, the size of the particles is controlled by the applied potential. In this instance, a more negative applied potential (−0.6 V) leads to the formation of smaller NPs, as evidenced by the samples C and D.

However, the time of the potential pulse mainly controls the coverage, as the maximum amount of Pd is detected in samples B and D (t = 20s) in comparison with the samples prepared at shorter times (5 s).

It should be noted that AFM tends to overestimate the lateral size of NPs due to tip convolution effects; however, firstly a sharp tip has been used (R_{tip} < 10 nm) and secondly, this systematic effect is present across all samples, and thus the relative size trend remains valid.

Regarding the oxygen content, the XPS survey analyses indicate that the O/Pd ratio decreases as the Pd coverage increases. Samples prepared at shorter deposition times (A and C, t = 5 s) exhibit higher oxygen content, reflecting a larger proportion of exposed oxygen-containing sites on the graphene substrate. Conversely, samples prepared at longer times (B and D, t = 20 s) show lower survey O/Pd ratios, consistent with greater Pd

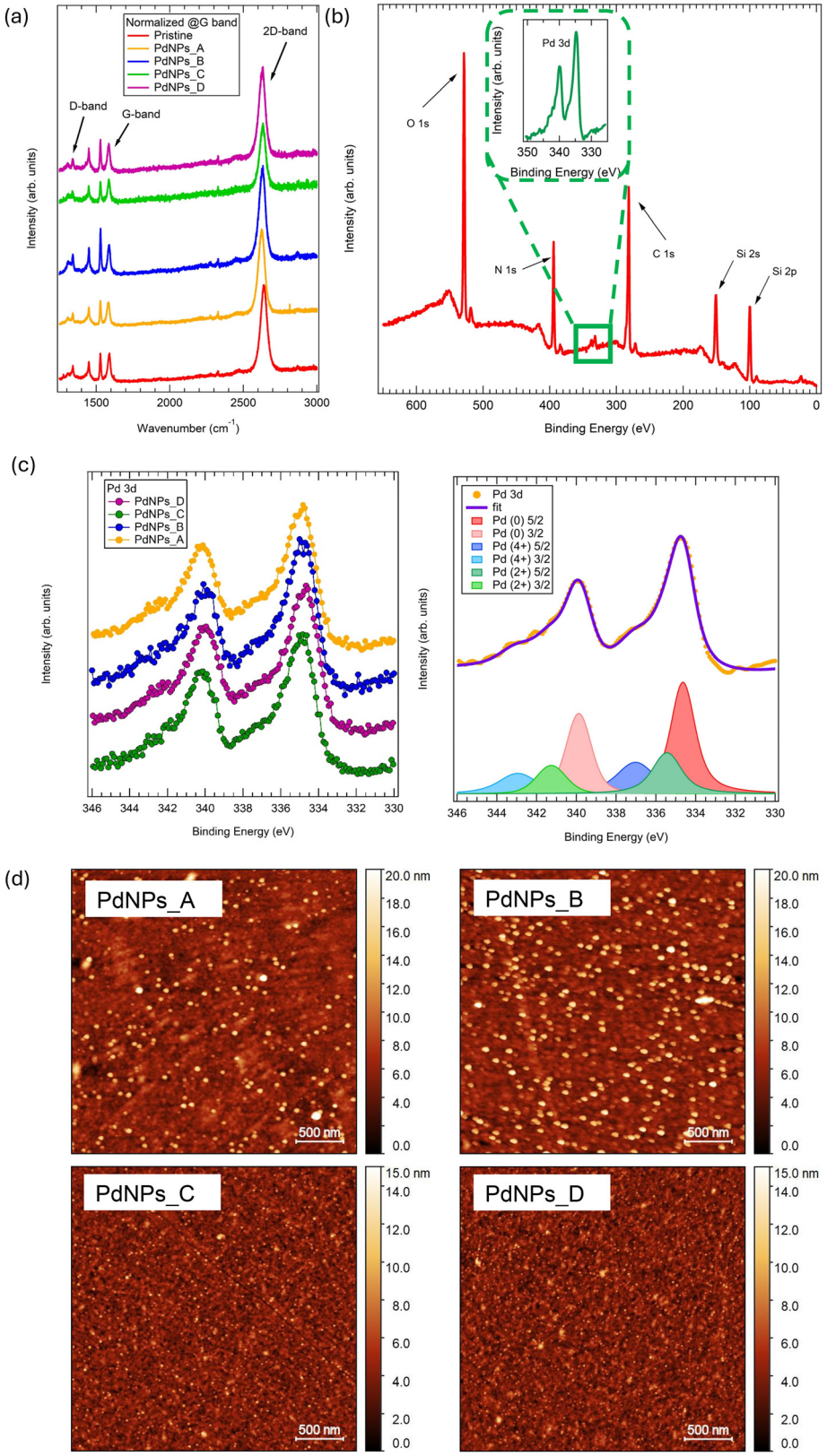

Fig. 1 (a) Raman spectra of pristine graphene (red trace) and the four decorated graphene layers. All the spectra are normalized at the G peak. (b) Representative XPS survey spectrum of a decorated graphene layer; inset: Pd 3d core-level spectrum. (c) Left-hand side: Pd 3d core-level spectra of the decorated samples. All the spectra present the same shape. Right-hand side: details of the Pd 3d core-level spectrum clearly indicating each contribution. (d) Representative AFM topography images of the decorated layers.

Table 1 Quantification analysis from XPS spectra and NP size distribution evaluated from several AFM images

Sample	XPS survey quantification	XPS survey quantification	XPS core-level quantification	AFM NP size (nm)
PdNPs_A	Pd : C = 0.010 : 1	Pd : O = 1 : 66.8	Pd : O = 1 : 0.55	36.1 ± 5.9
PdNPs_B	Pd : C = 0.025 : 1	Pd : O = 1 : 37.7	Pd : O = 1 : 0.68	47.5 ± 10.2
PdNPs_C	Pd : C = 0.015 : 1	Pd : O = 1 : 49.8	Pd : O = 1 : 0.50	25.5 ± 4.5
PdNPs_D	Pd : C = 0.030 : 1	Pd : O = 1 : 22.4	Pd : O = 1 : 0.58	19.5 ± 3.1

coverage reducing the exposed oxygen fraction. Interestingly, the core-level O/Pd values show only modest variation, suggesting that while the overall surface oxygen decreases with increasing Pd coverage, the oxygen atoms directly interacting with the Pd nanoparticles remain relatively constant. These observations highlight that the majority of the oxygen content is not related to the Pd NPs, and it is primarily influenced by the extent of the coverage, which is controlled by the deposition time, rather than by the applied potential. It is important to underline that this trend is consistent with the fact that electrochemical deposition occurs in an aqueous solution.

Finally, it is worth mentioning that the fraction of oxygen not linked to Pd NPs is partially ascribable to adventitious molecules physisorbed on the graphene surface. Indeed, as previously reported in the case of pristine graphene,[53,54] exposure to air leads to the adsorption of oxygen-containing species, such as C–O, C═O, and O–C═O groups. These species, however, are largely removed or significantly quenched upon mild annealing at 150 °C under ultra-high vacuum, confirming their physisorbed nature. Therefore, a portion of the oxygen detected in our samples, particularly in those with lower Pd coverage (A and C), can be attributed to similar adventitious adsorbates rather than to chemically bound oxygen associated with the Pd nanoparticles.

The NP-decorated surfaces and a pristine sample were exposed to ammonia, and an example of the responses collected for two selected concentrations (*i.e.* 0.92 ppm and 0.79 ppm) is reported in Fig. 2.

It is evident that at such low concentrations, pristine graphene exhibits a negligible response to ammonia. In contrast, for the decorated layers, exposure to ammonia determines a substantial resistance increase. This evidence confirms the p-type nature of the decorated samples, which is consistent with the concept that the electrons transferred from a reducing molecule, such as ammonia, decreases the number of holes in these layers.

It is important to note that our sensors do not reach saturation of the dynamical behaviour after exposures of 150 s (Fig. 2). This behaviour is not unusual at such low target gas concentrations, below 10 ppm, even for much longer exposure times (see for instance, Fig. 5g in ref. 55, Fig. 4c in ref. 56; Fig. 5a and Fig. 7c in ref. 57) Obviously, it is more likely to reach, or to get close to, a steady state for longer exposure times, though the use of sensing systems that need a very long time to show a flat dynamical curve becomes debatable. Finally, for a given sensor, saturation is often reached for high concentrations, while for low concentrations, curves similar to those shown in Fig. 2 are found (see, *e.g.* Fig. 7a and c in ref. 57).

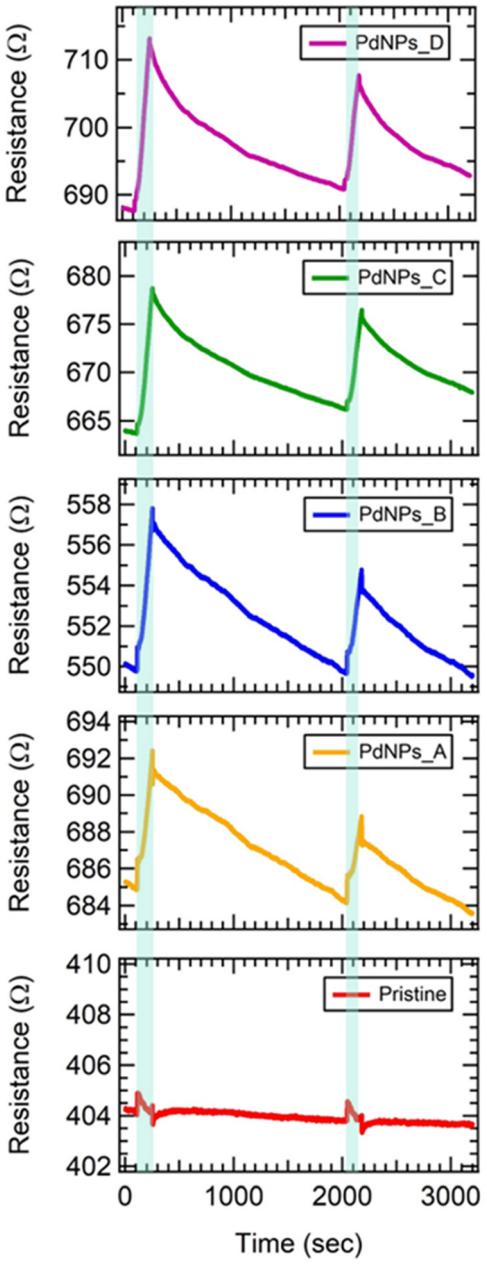

Fig. 2 Response of the sensor array exposed for 150 s to 0.92 and 0.79 ppm of ammonia. Exposure time is indicated by the shaded areas.

To obtain the calibration curves for all sensors (Fig. 3), several exposures at varying concentrations were conducted. A Freundlich isotherm ($\Delta R/R_0 = A[NH_3]^{pow}$) was used to model

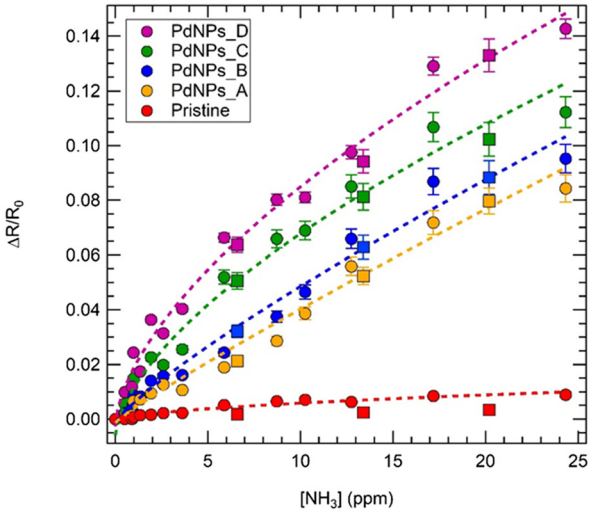

Fig. 3 Response of the sensors towards different ammonia concentrations, *i.e.* calibration curves. Dashed traces represent the Freundlich isotherm fitting; error bars are estimated considering the standard deviation of the mean response to 3 ammonia exposures collected at the same concentration. Circles: data collected with the as-prepared sensors; squares: data collected after 5 months from the sample preparation.

the data and the parameters obtained from the fit are reported in Table S1.

The calibration curves demonstrate a sublinear behaviour, a phenomenon that has been previously observed in the field of gas sensors based on carbon nanomaterials decorated with metal NPs.[58–60] A comparison of the calibration curves reveals that the decoration of graphene with Pd NPs enhances the response to ammonia. Additionally, it is observed that (i) the highest response is recorded for sample D, which contains the highest Pd content; (ii) smaller NPs appear to enhance the response more effectively (PdNPs_C and PdNPs_D); and (iii) greater coverage leads to better responses (PdNPs_D *vs.* PdNPs_C; PdNPs_B *vs.* PdNPs_A).

When comparing our calibration curves with those of similar systems for benchmarking purposes, it is important to be aware that the calibration curve obtained from dynamical curves before saturation underestimates the response (which is expected to be higher at a steady state). Therefore, the present results can be considered a lower limit for sensitivity. This approach avoids overclaiming of performances in terms of sensitivity.

Regarding the detection limit (dl), estimated using the following formula, $3[NH_3]/((R - R_0)/\sigma)$,[14,61] where σ is the electrical signal fluctuation evaluated on an average basis considering the baseline signal, the detection limit has been found to be in the ppb range for all the samples, with lower limits observed for the decorated layers with respect to the pristine one. Specifically, the detection limits for ammonia are 6 ppb, 13 ppb, 32 ppb, and 42 ppb, for PdNPs_D, PdNPs_C, PdNPs_B and PdNPs_A, respectively. In comparison, the pristine graphene detection limit is 380 ppb. The evaluated detection limits are among the best reported in the literature to date (see Table S2). Of note, due to the sublinear nature of the calibration curves, the 0–2 ppm range, which can be assumed as linear, has been considered to evaluate the detection limits.

Regarding the ammonia range investigated, it is noteworthy that the dynamic NH_3 range aligns with the requirements for medical, environmental and safety applications, specifically within the low- or sub-ppm range (refer to Table S2).[7,9,62,63]

Response and recovery times are in line with what has been reported so far for graphene-based chemiresistors (Table S2).

Finally, the sensitivity parameter, which is defined as $S = 100 \times (\Delta R/R_0)/[NH_3]$, has been used for a comparison with the existing literature data. It is noteworthy that the benchmarking was conducted exclusively on papers that declared gas concentration and sensor response/sensitivity, working as chemiresistors at room temperature.

The benchmarking, reported in Fig. 4, demonstrates that the present results, which are primarily obtained in a range of low concentrations of NH_3, often surpass the results on graphene chemiresistor sensors reported to date in the literature.[14,64–80]

Selectivity, reproducibility and stability have also been investigated. The stability and reproducibility of the sensor response towards ammonia detection have been demonstrated, with results clearly showing excellent stability and reproducibility for up to five months after sample functionalization (see Fig. 3, square symbols).

A quantitative comparison of the calibration curves recorded after 5 months (Fig. 3, square symbols) with the one

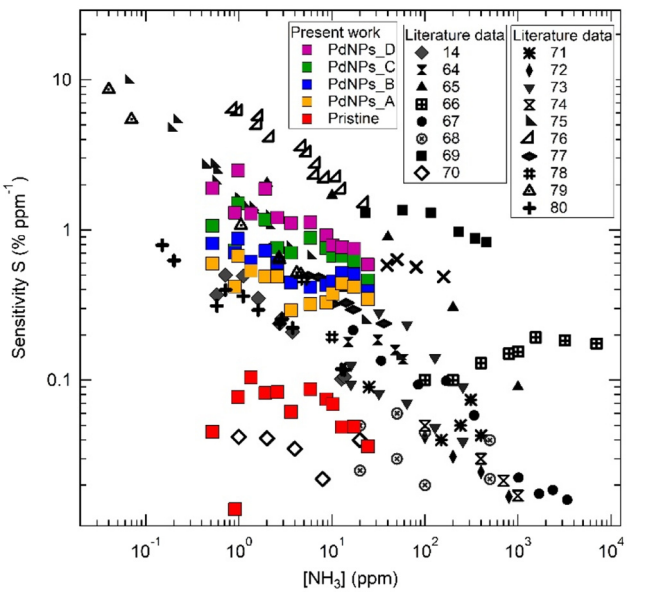

Fig. 4 Benchmarking for sensitivity S ($S = (\Delta R/R_0 \times 100)/[NH_3]$) towards ammonia exposure of the decorated samples (blue, green, purple and yellow squares) compared to pristine graphene (red squares) and to other chemiresistors based on graphene (pristine and/or functionalized) presented in the literature (black symbols).[14,64–80] A log–log scale has been used for clarity to present the data.

drawn just after sample preparation (Fig. 3, circles) revealed that the variation in response at each concentration was within ±5% for all Pd-decorated layers, with no measurable drop in sensitivity or increase in the detection limit. This demonstrates that the sensing performance remains stable for at least 5 months or more, under ambient laboratory conditions.

With regards to selectivity, exposures to ethanol, acetone, water vapor, 2-propanol and nitrogen dioxide have been performed.

Incidentally, it is important to mention that all of the tested gases are classified as interfering gases and are pertinent to a variety of applications, including breath analysis, environmental assessment, safety and food quality monitoring. Indeed, recently, ethanol has gained considerable attention as a biofuel due to its relatively lower carbon dioxide emissions compared to fossil fuels. However, incomplete combustion of ethanol leads to an increase in smog levels.[81] Ethanol is also related to the presence of rotten fruits and vegetables,[82,83] while both ethanol and 2-propanol have been identified as two lung cancer biomarkers.[84] Acetone, on the other hand, is emitted by rotten meat, mouldy bread, and generally carbohydrates.[85] Its presence in exhaled breath is notably elevated in patients affected by diabetes and ketoacidosis.[86,87]

Finally, water vapor exposure has been studied for various applications, including breathomics, where the sensors must work and be stable in the presence of a relative humidity (R. H.) value of 100%.

A comparison of the sensor responses revealed that the decorated sensors exhibited superior selectivity for ammonia over the other tested gases at room temperature as shown in Fig. 5. This figure presents the sensor array responses, $\Delta R/R_0$, to the selected target molecules. The response to high concentrations of these potential interfering gases is minimal and negligible when compared to the response towards trace amounts of ammonia, *i.e.*, few parts per million (ppm). Considering nitrogen dioxide, the response is not completely negligible. However, the distinction between the two gases is evident from their opposite response signs, as would be expected. Nitrogen dioxide, being an oxidizing gas, and ammonia, being a reducing agent, exhibit divergent responses. The enhancement of the response, attributable to the decoration of Pd NPs, exhibits a high degree of selectivity. This is evidenced by the observation that the response of the four samples decorated with Pd NPs to NO_2 is analogous to the response of the pristine sample. The results substantiate the hypothesis that Pd NP-decorated graphene sensors exhibit a high degree of selectivity towards ammonia.

In order to elucidate the reason behind the difference in response, $\Delta R/R_0$, the interaction of the studied molecules with the substrate was evaluated through DFT calculations.

The Pd NP-decorated graphene sensor response is based on changes in the graphene resistance, which are caused by the Pd work function change.[88,89] Typically, CVD graphene acts as a p-type semimetal.[90] When graphene is decorated with Pd NPs, its resistance decreases because the Pd work function (5.05 eV) is greater than that of graphene (4.83 eV). This causes electron transfer from the graphene layer to the Pd NPs, increasing the hole density in the p-type graphene.

On the other hand, when a molecule is adsorbed on Pd NPs, the Pd WF undergoes modification, which in turn affects the electronic behaviour of graphene, leading to an increase or decrease in hole density in graphene (see Table 2 and Fig. 6).

The binding energy of all molecules studied is provided in Table 2, and in all cases, this interaction is exothermic.

When Pd NP-decorated graphene is exposed to ammonia gas, the work function is smaller (2.18 eV) than that of graphene (4.83 eV) and the graphene resistance increases due to

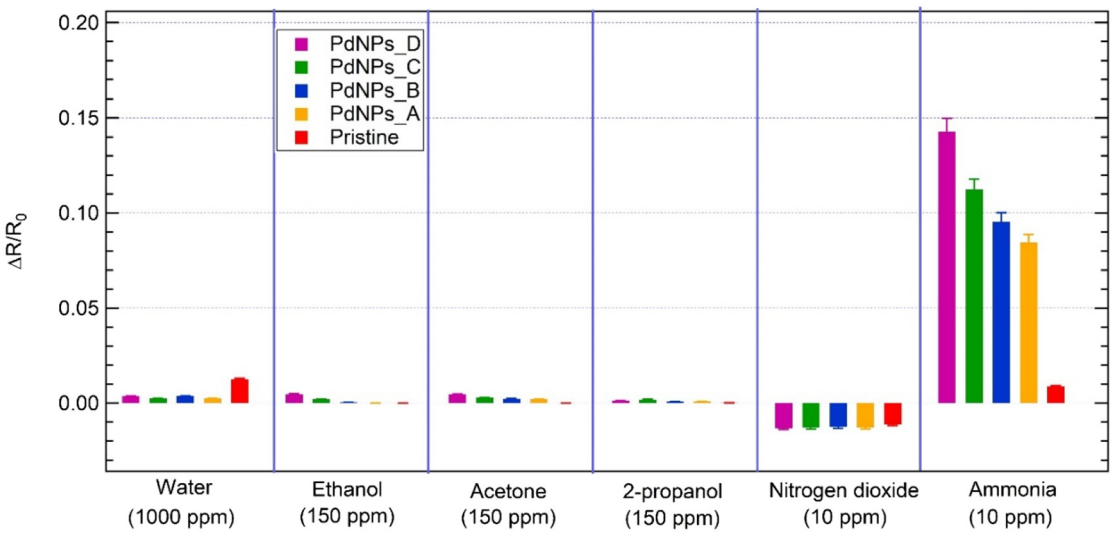

Fig. 5 Responses to different target gas molecules, water vapour (1000 ppm), ethanol, acetone, and 2-propanol (150 ppm), nitrogen dioxide and ammonia (10 ppm), on the pristine sample (red) and the decorated layers (green, blue, purple and yellow).

Table 2 Theoretical data of binding energy

	Water	Ethanol	Acetone	2-Propanol	NO_2	NH_3
E_b/eV	−0.34	−0.62	−0.52	−0.75	−1.70	−0.69
ΔWF/eV	−0.14	−1.28	−1.01	−0.84	+1.61	−2.65

E_b, and the change in the work function with respect to the graphene surface, $\Delta WF = WF - WF_{graphene}$. A side view of each system is included.

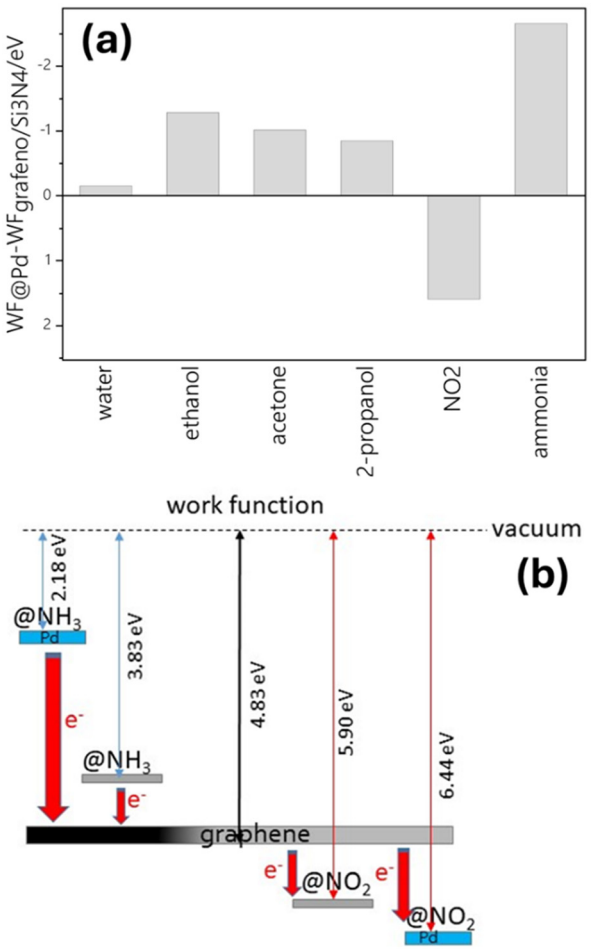

Fig. 6 (a) Difference between the work function of the different gas molecules adsorbed on the Pd surface and the work function of graphene on Si_3N_4. (b) Diagram showing the work functions of NH_3 (left) and NO_2 (right) adsorbed on graphene on Si_3N_4 and on palladium. Of note: *NO_2 (μ-N,O) (nitrite adsorption on Pd(111) more stable[91]).

the electron transfer from the Pd NPs to the graphene, reducing the p-type holes in the graphene. On the other hand, in the presence of NO_2 gas, the work function increases to 6.44 eV, surpassing that of graphene, and the resistance decreases due to the electron transfer from the graphene to the Pd NPs, thereby increasing the p-type holes in the graphene electronic structure. The remaining gases studied were optimized (Fig. 6a), demonstrating a correlation between the change in the work function and the sign of the sensing response.

The binding energies of the main analytes, namely NH_3 and NO_2, have also been calculated for pristine graphene. The values for the adsorption energy of NH_3 and NO_2 are −0.10 eV and −0.18 eV, respectively. These values are lower than the ones found on the palladium surface (−0.69 eV for NH_3 and −1.70 eV for NO_2), showing a preferential adsorption on the palladium surface compared to the graphene one.

In order to understand the enhancement in the response to ammonia compared to that of NO_2 when palladium is electrodeposited onto the graphene surface, a comparison of the WF change in the case of graphene on Si_3N_4 and palladium surfaces after the adsorption of these molecules was carried out (see Fig. 6b and Fig. S4). As can be observed, the change in the work function upon ammonia adsorption is approximately threefold larger for palladium compared to the graphene. However, the change in the case of NO_2 adsorption is comparable for both surfaces. These results are in good agreement, at least qualitatively, with the enhancement observed in the experimental results. Finally, it is worth investigating the effect of humidity on the sensing properties of the layers, as water vapor is one of the strongest interferents during gas sensing.

The negligible resistance variation upon exposure to 1000 ppm water vapor (equivalent to ~5% additional R.H.; Fig. 5) indicates that humidity exerts minimal influence under our test conditions. This observation aligns with DFT results, which show that water induces only a negligible change in work function compared to ammonia (Fig. 6). We can therefore conclude that the sensors are expected to maintain stable performance even in environments with varying humidity.

Conclusions

In this study, a straightforward and economical approach for decorating graphene with NPs for the selective enhancement of ammonia sensing is presented.

Palladium NP-decorated graphene has been produced through electrodeposition, a method that allows for the precise control of both the number and the size of the particles by adjusting the applied time and potential, respectively. The presence of well-defined particles on the graphene surface is confirmed through AFM and XPS analysis. Raman spectra indicated that the graphene single layer remained undamaged, and the D band present in the spectra is analogous to that observed in bare graphene following palladium electrodeposition.

Ammonia exposure tests were performed, and calibration curves for each sensor were drawn. The sensors exhibited excellent sensitivity, response and recovery times consistent with previously reported values for graphene chemiresistors. The stability of all sensors over a period of five months was ascertained, and noteworthy detection limit values were revealed. Exposures to acetone, 2-propanol, ethanol, and water vapor were conducted, thereby proving the selectivity of the sensors and disclosing a selective enhancement of the response to ammonia for the decorated graphene sensors in comparison with the pristine surface. A systematic study of the effect of Pd NP size and coverage on ammonia sensing revealed that smaller NPs enhance ammonia sensing more effectively, while higher coverage leads to better performance in samples with the same NP size. This suggests the potential for further development of competitive Pd NP-decorated sensors.

In order to gain insight into the mechanism of the Pd NP-decorated graphene, DFT calculations of the adsorption of the different molecules were carried out. The potential change in the resistance of the graphene was analysed through the change in the work function after the electrodeposition. It is observed that the work function of Pd (5.05 eV) is greater than that of the graphene on Si_3N_4 (4.83 eV). Consequently, electron transfer from graphene to Pd NPs enhances the hole density in p-type graphene. The experimental study of the adsorption of the gases under investigation revealed a correlation between the change in the work function and the sign of the sensing response. The enhancement of the ammonia response compared to that of the nitrogen dioxide has been studied through DFT calculations of the work function change of graphene and palladium surfaces upon adsorption of the gas molecules. The greater WF change due to ammonia adsorption reveals that the enhancement is related to the more significant change induced in the Pd WF due to ammonia adsorption compared to other gases.

Conflicts of interest

There are no conflicts to declare.

Data availability

The data supporting this article are partially included in the supplementary information (SI) or are available upon request from the authors.

Supplementary information is available. See DOI: https://doi.org/10.1039/d5nr02547h.

Acknowledgements

S. F. acknowledges Fondazione Cariplo for financial support, within the grant BREATH-SENSE 2023-1506 – 'Giovani Ricercatori 2023'.

M. C. R. G. acknowledges the University of La Laguna (ULL) for a María Zambrano fellowship and the research Vicerrectorate of ULL for funding through a research project for novel professors in 2022.

M. C. R. G. and A. H. C. acknowledge the Canarian Agency for Research, Innovation and Information Society (ACIISI) for funding in the scope of the project PROID2024010029, cofounded by the European Regional Development Fund (FEDER Canary Islands Program 2021-2027). Support from the Cabildo de Tenerife-TALENTUM TIA (Exp. 2024/0002355) programme is gratefully acknowledged.

References

1 M. Insausti, R. Timmis, R. Kinnersley and M. C. Rufino, *Sci. Total Environ.*, 2020, **706**, 135124.
2 I. Zahoor and A. Mushtaq, *Int. J. Chem. Biol. Sci.*, 2023, **23**, 164–176.
3 N. T. Brannelly, J. P. Hamilton-Shield and A. J. Killard, *Crit. Rev. Anal. Chem.*, 2016, **46**(6), 490–501.
4 J. Malecek and J. J. Tufano, *Strength Cond. J.*, 2021, **43**(6), 76–86.
5 A. N. Hristov, *J. Dairy Sci.*, 2011, **94**(6), 3130–3136.
6 M. Kruse and J. N. B. Bell, *Atmos. Environ.*, 1987, **21**(9), 1939–1946.
7 S. Matindoust, A. Farzi, M. Baghaei Nejad, M. H. Shahrokh Abadi, Z. Zou and L. R. Zheng, *J. Mater. Sci.: Mater. Electron.*, 2017, **28**, 7760–7768.
8 P. P. Ricci and O. J. Gregory, *Sci. Rep.*, 2021, **11**(1), 7185.
9 S. Freddi, A. V. Emelianov, I. I. Bobrinetskiy, G. Drera, S. Pagliara, D. S. Kopylova, M. Chiesa, G. Santini, N. Mores, U. Moscato, A. G. Nasibulin, P. Montuschi and L. Sangaletti, *Adv. Healthcare Mater.*, 2020, **9**(12), 2000377.
10 S. S. Varghese, S. Lonkar, K. K. Singh, S. Swaminathan and A. Abdala, *Sens. Actuators, B*, 2015, **218**, 160–183.
11 R. Bogue, *Sens. Rev.*, 2014, **34**(1), 1–8.
12 T. Wang, D. Huang, Z. Yang, *et al.*, *Nano-Micro Lett.*, 2016, **8**, 95–119.
13 S. Freddi, M. C. Rodriguez Gonzalez, A. Casotto, L. Sangaletti and S. De Feyter, *Chem. – Eur. J.*, 2023, **29**(60), e202302154.
14 S. Freddi, C. Marzuoli, S. Pagliara, G. Drera and L. Sangaletti, *RSC Adv.*, 2023, **13**(1), 251–263.
15 Z. D. Leve, E. I. Iwuoha and N. Ross, *Materials*, 2022, **15**(4), 1326.
16 R. Ghosh, M. Aslam and H. Kalita, *Mater. Today Commun.*, 2022, **30**, 103182.
17 N. M. Nurazzi, N. Abdullah, S. Z. Demon, N. A. Halim, A. F. Azmi, V. F. Knight and I. S. Mohamad, *Nanotechnol. Rev.*, 2021, **10**(1), 330–369.
18 N. S. Struchkov, A. V. Romashkin, M. K. Rabchinskii, S. D. Saveliev, P. D. Cherviakova, R. G. Chumakov, *et al.*, *Sens. Actuators, B*, 2024, **417**, 136088.
19 M. K. Rabchinskii, V. V. Sysoev, M. Brzhezinskaya, M. A. Solomatin, V. S. Gabrelian, D. A. Kirilenko, *et al.*, *Nanomaterials*, 2024, **14**(9), 735.

20 M. Gupta, H. F. Hawari, P. Kumar, Z. A. Burhanudin and N. Tansu, *Nanomaterials*, 2021, **11**(3), 623.
21 S. B. Kang, A. Sanger, M. H. Jeong, J. M. Baik and K. J. Choi, *Sens. Actuators, B*, 2024, **379**, 133196.
22 D. H. Shin, Y. S. Choi, S. Y. Park, C. S. Yeo, Y. Y. Park, J. Y. Song, *et al.*, *Appl. Surf. Sci.*, 2022, **578**, 151832.
23 E. Dilonardo, M. Penza, M. Alvisi, R. Rossi, G. Cassano, C. Di Franco, *et al.*, *Beilstein J. Nanotechnol.*, 2017, **8**(1), 592–603.
24 S. M. Iordache, E. I. Ionete, A. M. Iordache, E. Tanasa, I. Stamatin and C. E. A. Grigorescu, *Int. J. Hydrogen Energy*, 2021, **46**(18), 11015–11024.
25 S. J. Kim, Y. J. Park, E. J. Ra, K. K. Kim, K. H. An, Y. H. Lee, J. Y. Choi, C. H. Park, S. K. Doo, M. H. Park and C. W. Yang, *Appl. Phys. Lett.*, 2007, **90**, 023114.
26 K. Wetchakun, T. Samerjaia, N. Tamaekong, C. Liewhiran, C. Siriwong, C. Kruefu, A. Wisitsoraat, A. Tuantranont and S. Phanichphant, *Sens. Actuators, B*, 2011, **160**, 580–591.
27 S. Ju, J. M. Lee, Y. Jung, E. Lee, W. Lee and S. J. Kim, *Sens. Actuators, B*, 2010, **146**(1), 122–128.
28 B. Alfano, E. Massera, T. Polichetti, M. L. Miglietta and G. Di Francia, *Sens. Actuators, B*, 2017, **253**, 1163–1169.
29 R. D. Martínez-Orozco, R. Antaño-López and V. Rodríguez-González, *New J. Chem.*, 2015, **39**(10), 8044–8054.
30 M. C. R. González, A. G. Orive, R. C. Salvarezza and A. H. Creus, *Phys. Chem. Chem. Phys.*, 2016, **18**(3), 1953–1960.
31 M. C. R. González, L. M. Rivera, E. Pastor, A. H. Creus and G. García, *J. Catal.*, 2018, **366**, 1–7.
32 G. Drera, G. Salvinelli, J. Åhlund, P. G. Karlsson, B. Wannberg, E. Magnano, S. Nappini and L. Sangaletti, *J. Electron Spectrosc. Relat. Phenom.*, 2014, **195**, 109.
33 G. Drera, C. M. Kropf and L. Sangaletti, *Mach. Learn.: Sci. Technol.*, 2020, **1**, 015008.
34 Gwyddion, accessed: July, 2023, https://gwyddion.net/.
35 G. Kresse and D. Joubert, *Phys. Rev. B:Condens. Matter Mater. Phys.*, 1999, **59**, 1758–1775.
36 G. Kresse and J. Hafner, *Phys. Rev. B:Condens. Matter Mater. Phys.*, 1993, **47**, 558–561.
37 G. Kresse and J. Furthmüller, *Comput. Mater. Sci.*, 1996, **6**, 15–50.
38 G. Kresse and J. Furthmüller, *Phys. Rev. B:Condens. Matter Mater. Phys.*, 1996, **54**, 11169–11186.
39 B. Hammer, L. B. Hansen and J. K. Nørskov, *Phys. Rev. B: Condens. Matter Mater. Phys.*, 1999, **59**, 7413.
40 S. Grimme, *J. Comput. Chem.*, 2006, **27**, 1787–1799.
41 S. Grimme, J. Antony, S. Ehrlich and H. Krieg, *J. Chem. Phys.*, 2010, **132**, 154104.
42 W. B. Pearson, *A Handbook of Lattice Spacings and Structures of Metals and Alloys*, Pergamon Press, 1958.
43 H. J. Monkhorst and J. D. Pack, *Phys. Rev. B*, 1976, **13**, 5188–5192.
44 A. C. Ferrari and D. M. Basko, *Nat. Nanotechnol.*, 2013, **8**, 235–246.
45 J. H. Bong, O. Sul, A. Yoon, S. Y. Choi and B. J. Cho, *Nanoscale*, 2014, **6**, 8503–8508.
46 A. R. Chourasia and D. R. Chopra, *Surf. Sci. Spectra*, 1993, **2**(2), 117–122.
47 G. Ambrosio, A. Brown, L. Daukiya, G. Drera, G. Di Santo, L. Petaccia, S. De Feyter, L. Sangaletti and S. Pagliara, *Nanoscale*, 2020, **12**(16), 9032–9037.
48 S. Yang, J. Dong, Z. Yao, C. Shen, X. Shi, *et al.*, *Sci. Rep.*, 2014, **4**(1), 4501.
49 T. Shobha, C. L. Aravinda, P. Bera, L. G. Devi and S. M. Mayanna, *Mater. Chem. Phys.*, 2003, **80**, 656–661.
50 X. Yang, M. Zhen, G. Li, X. Liu, X. Wang, C. Shu, *et al.*, *J. Mater. Chem. A*, 2013, **1**(28), 8105–8110.
51 L. S. Kibis, A. I. Titkov, A. I. Stadnichenko, S. V. Koscheev and A. I. Boronin, *Appl. Surf. Sci.*, 2009, **255**, 9248–9254.
52 O. Lupan, V. Postica, M. Hoppe, N. Wolff, O. Polonskyi, T. Pauportè, B. Viana, O. Majérus, L. Kienle, F. Faupel and R. Adelung, *Nanoscale*, 2018, **10**(29), 14107–14127.
53 M. Zanotti, S. Freddi and L. Sangaletti, *Adv. Mater. Technol.*, 2025, **10**(3), 2400985.
54 A. Casotto, G. Drera, D. Perilli, S. Freddi, S. Pagliara, M. Zanotti, L. Schio, A. Verdini, L. Floreano, C. di Valentin and L. Sangaletti, *Nanoscale*, 2022, **14**(36), 13166–13177.
55 C. W. Lee, T. H. Eom, S. H. Cho and H. W. Jang, *Adv. Sens. Res.*, 2023, **2**(9), 2200057.
56 Y. Kim, T. Kim, J. Lee, Y. S. Choi, J. Moon, S. Y. Park, *et al.*, *Adv. Mater.*, 2021, **33**(2), 2004827.
57 Y. SeokáChoi, S. YunáPark, T. HyungáLee, C. WooáMoon, B. HeeáHong and H. WonáJang, *Nanoscale*, 2019, **11**(6), 2966–2973.
58 S. Freddi, G. Drera, S. Pagliara, A. Goldoni and L. Sangaletti, *Analyst*, 2019, **144**(13), 4100–4110.
59 H. Song, X. Li, P. Cui, S. Guo, W. Liu and X. Wang, *Sens. Actuators, B*, 2017, **244**, 124–130.
60 I. Karaduman, E. Er, H. Çelikkan, N. Erk and S. Acar, *J. Alloys Compd.*, 2017, **722**, 569–578.
61 D. Kumar, P. Chaturvedi, P. Saho, P. Jha, A. Chouksey, M. Lal, *et al.*, *Sens. Actuators, B*, 2017, **240**, 1134–1140.
62 M. Chiesa, F. Rigoni, M. Paderno, P. Borghetti, G. Gagliotti, M. Bertoni, *et al.*, *J. Environ. Monit.*, 2012, **14**(6), 1565–1575.
63 A. A. Nair and F. Yu, *Atmosphere*, 2020, **11**(10), 1092.
64 M. Gautam and A. H. Jayatissa, *Solid-State Electron.*, 2012, **78**, 159–165.
65 F. Yavari, E. Castillo, H. Gullapalli, P. M. Ajayan and N. Koratkar, *Appl. Phys. Lett.*, 2012, **100**, 203120.
66 Z. Wu, X. Chen, S. Zhu, Z. Zhou, Y. Yao, W. Quan and B. Liu, *Sens. Actuators, B*, 2013, **178**, 485–493.
67 Y. Seekaew, D. Phokharatkul, A. Wisitsoraat and C. Wongchoosuk, *Appl. Surf. Sci.*, 2017, **404**, 357–363.
68 Z. Ben Aziza, Q. Zhang and D. Baillargeat, *Appl. Phys. Lett.*, 2014, **105**, 254102.
69 C. Xiang, D. Jiang, Y. Zou, H. Chu, S. Qiu, H. Zhang, F. Xu, L. Sun and L. Zheng, *Ceram. Int.*, 2015, **41**, 6432–6438.
70 R. Lv, G. Chen, Q. Li, A. McCreary, A. Botello-Mendez, S. V. Morozov, L. Liang, X. Declerck, N. Perea-Lopez, D. A. Cullen, S. Feng, A. L. Elias, R. Cruz-Silva, K. Fujisawa, M. Endo, F. Kang, J.-C. Charlier, V. Meunier, M. Pan,

A. R. Harutyunyan, K. S. Novoselov, M. Terrones, *et al.*, *Proc. Natl. Acad. Sci. U. S. A.*, 2015, **112**(47), 14527–14532.
71 D. Wu, Q. Peng, S. Wu, G. Wang, L. Deng, H. Tai, L. Wang, Y. Yang, L. Dong, Y. Zhao, J. Zhao, D. Sun and L. Lin, *Sensors*, 2018, **18**, 4405.
72 T. Liang, R. Liu, C. Lei, K. Wang, Z. Li and Y. Li, *Micromachines*, 2020, **11**, 965.
73 S. Srivastava, S. K. Jain, G. Gupta, T. D. Senguttuvan and B. K. Gupta, *RSC Adv.*, 2020, **10**, 1007.
74 Y. Zhu, L. Yu, D. Wu, W. Lv and L. Wang, *Sens. Actuators, A*, 2021, **318**, 112434.
75 S. Freddi, M. C. R. Gonzalez, P. Carro, L. Sangaletti and S. De Feyter, *Angew. Chem., Int. Ed.*, 2022, **61**(16), e202200115.
76 S. Freddi, D. Perilli, L. Vaghi, M. Monti, A. Papagni, C. Di Valentin and L. Sangaletti, *ACS Nano*, 2022, **16**(7), 10456–10469.
77 S. Freddi, M. Vergari, S. Pagliara and L. Sangaletti, *Sensors*, 2023, **23**, 882.
78 S. Freddi, *Il Nuovo Cimento*, 2023, **46C**, 125.
79 D. Perilli, S. Freddi, M. Zanotti, G. Drera, A. Casotto, S. Pagliara, L. Schio, L. Sangaletti and C. Di Valentin, *Commun. Mater.*, 2024, **5**(1), 254.
80 S. Freddi, L. Vaghi, A. Penoni, L. Scapinello and L. Sangaletti, *Chemosensors*, 2025, **13**(5), 165.
81 J. D. Willey, G. B. Avery, J. D. Felix, R. J. Kieber, R. N. Mead and M. S. Shimizu, *npj Clim. Atmos. Sci.*, 2019, **2**(1), 1–5.
82 K. Balasubramanian, V. Ambikapathy and A. Panneerselvam, *J. Microbiol. Biotechnol. Res.*, 2011, **1**(4), 158–163.
83 R. SatishBabu, S. Rentala, M. L. Narsu, Y. Prameeladevi and D. G. Rao, *Int. J. Biotechnol. Biochem.*, 2010, **6**(3), 351–358.
84 S. Nag, A. Sachan, M. Castro, V. Choudhary and J. F. Feller, *J. Mater. Chem. B*, 2017, **5**, 348.
85 N. E. Poe, D. Yu, Q. Jin, M. A. Ponder, A. C. Stewart, J. A. Ogejo, H. Wang and H. Huang, *Waste Manage.*, 2020, **107**, 150–158.
86 G.-T. Fan, C.-L. Yang, C.-H. Lin, C.-C. Chen and C.-H. Shih, *Talanta*, 2014, **120**, 386.
87 C. Turner, C. Walton, S. Hoashi and M. Evans, *J. Breath Res.*, 2009, **3**, 046004.
88 R. S. Sundaram, C. Gómez-Navarro, K. Balasubramanian, M. Burghard and K. Kern, *Adv. Mater.*, 2008, **20**(16), 3050–3053.
89 J. Kong, M. G. Chapline and H. Dai, *Adv. Mater.*, 2001, **13**(18), 1384–1386.
90 J. E. Scheerder, T. Picot, N. Reckinger, T. Sneyder, V. S. Zharinov, J. F. Colomer, *et al.*, *Nanoscale*, 2017, **9**(29), 10494–10501.
91 R. B. Getman and W. F. Schneider, *J. Phys. Chem. C*, 2007, **111**(1), 389–397.